ACS APPLIED MATERIALS & INTERFACES

Research Article

www.acsami.org

Comprehensive Structural, Surface-Chemical and Electrochemical Characterization of Nickel-Based Metallic Foams

Julia van Drunen,[†] Brandy Kinkead,[‡] Michael C. P. Wang,[‡] Erwan Sourty,[§] Byron D. Gates,[‡] and Gregory Jerkiewicz*,[†]

[†]Department of Chemistry, Queen's University, 90 Bader Lane, Kingston ON, K7L 3N6, Canada

[‡]Department of Chemistry and 4D LABORATORIES, Simon Fraser University, 8888 University Drive, Burnaby BC, V5A 1S6, Canada

[§]FEI Company, NanoPort, Achtseweg Noord 5, Bldg, 5651 GG, Eindhoven, The Netherlands

Supporting Information

ABSTRACT: Nickel-based metallic foams are commonly used in electrochemical energy storage devices (rechargeable batteries) as both current collectors and active mass support. These materials attract attention as tunable electrode materials because they are available in a range of chemical compositions, pore structures, pore sizes, and densities. This contribution presents structural, chemical, and electrochemical characterization of Ni-based metallic foams. Several materials and surface science techniques (transmission electron microscopy (TEM), scanning electron microscopy (SEM), energy dispersive spectrometer (EDS), focused ion beam (FIB), and X-ray photoelectron spectroscopy (XPS)) and electrochemical methods (cyclic voltammetry (CV)) are used to examine the micro-, meso-, and nanoscopic structural characteristics, surface morphology, and surface-chemical composition of these materials. XPS combined with Ar-ion etching is employed to analyze the surface and near-surface chemical composition of the foams. The specific and electrochemically active surface areas (A_s, A_{ecsa}) are determined using CV. Though the foams exhibit structural robustness typical of bulk materials, they have large A_s, in the range of 200−600 $cm^2\ g^{-1}$. In addition, they are dual-porosity materials and possess both macro- and mesopores.

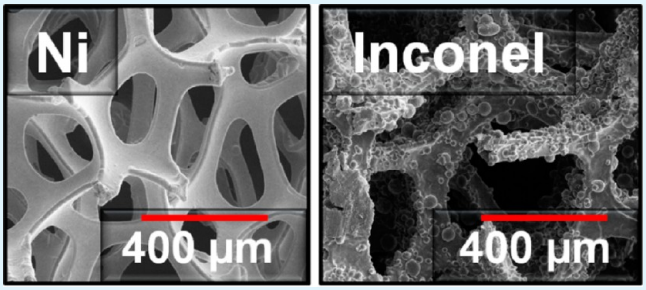

KEYWORDS: *nickel foam, real surface area, dual-porosity materials, chemical etching, focused ion beam, nickel-based electrocatalysts*

INTRODUCTION

Nickel is an important metal applied in various industries due to several desirable physical, metallurgical, and chemical properties (e.g., excellent electrical and thermal conductivities, malleability, ductility, ability to form stable alloys with different transition metals, corrosion resistance in alkaline and saline media). It is widely used in energy-storing and energy-delivering devices, such as rechargeable batteries,[1] alkaline fuel cells,[2] and electrochemical supercapacitors.[3,4] Nickel alloys and superalloys were developed specifically to exhibit excellent stability in harsh environments[5] (corrosive, high temperature, and high stress). Nickel oxides were showed to be effective catalysts for the electro-oxidation of alcohols and amines.[6,7] In all of these applications, the surface chemistry of the Ni-based material impacts the performance, catalytic activity, efficiency, and stability.[4,8,9]

Porous metallic materials possessing high specific surface area (A_s in $cm^2\ g^{-1}$) offer a beneficial combination of properties such as large surface area for heterogeneous catalysis, low material usage, low mass density, and ease of manufacture. There are several methods of manufacturing open-pore metallic materials, such as foaming of metal melts, powder compaction and melting, chemical vapor deposition (CVD), physical vapor deposition (PVD), and electrochemical deposition of one or several metals on a preformed, open-pore substrate.[10−12]

Nickel foams are prepared in two stages: (step 1) CVD of Ni by the decomposition of $Ni(CO)_4$ on an open-cell polyurethane substrate and (step 2) a high temperature (~1000 °C) burnout of the polymeric template together with sintering and annealing of the Ni deposit.[12] A variation of the process involves the formation of a thin Ni layer through PVD on a polyurethane substrate, followed by electrodeposition of Ni to thicken the struts. Multicomponent foams (see Table 1 for their chemical composition) are produced through a powder metallurgical process, which involves spraying of premade Ni foam with a binding agent followed by coating with a powder containing several metals. The final stage is heat treatment at a selected temperature, which results in sintering and interdiffusion of the component metals.[13] Such produced Ni foams are used to manufacture rechargeable batteries[10] and electro-

Received: April 30, 2013
Accepted: June 11, 2013
Published: June 11, 2013

   dx.doi.org/10.1021/am401606n | ACS Appl. Mater. Interfaces 2013, 5, 6712−6722

Table 1. Structural Characteristics of Ni-Containing Foams

chemical composition	sheet density (g m^{-2})	bulk density (g cm^{-3})	range of grain size (μm)	average strut wall thickness (μm $\pm$ σ μm)	thickness of innerwall structure (μm)
Ni	320	0.16	1−12	2.5 ± 0.5	0.3
Ni	420	0.21	1−12	2.5 ± 0.5	0.2
Ni	510	0.26	4−12	3.5 ± 0.5	0.2
Ni	640	0.32	4−12	4.0 ± 1.0	0.3
NiCrMoFeNbTa (Inconel)	1320	0.66	4−20	6.0 ± 2.0	0.7
NiFeCrAl (FE2)	1200	0.60	4−20	5.0 ± 1.0	0.6

chemical supercapacitors,[12] optically transparent electrodes,[14] and permeable electrodes for flow electrolysis systems.[2,10] The multicomponent foams examined in this study were developed specifically for elevated temperature, highly corrosive, and strongly oxidizing environments (e.g., diesel engine particulate filters).[13] The Inconel 625 alloy (Table 1) was designed to offer acid resistance and high temperature stability, whereas the FE2 alloy (Table 1) was designed to withstand oxidation at high temperatures.[13]

This study presents a structural, surface, and electro-chemical characterization of open-cell Ni and Inconel foams using scanning and transmission electron microscopies (SEM, TEM), focused ion beam (FIB), X-ray photoelectron spectroscopy (XPS), and cyclic voltammetry (CV). It discusses the applicability of chemical etching as a means of removing a native oxide layer, increasing the surface area, and activating the electrode toward a specific electrochemical reaction without compromising the integrity of three-dimensional (3D) structure.

EXPERIMENTAL SECTION

Electrochemical Measurements. Electrochemical measurements were carried out using a two-compartment Pyrex electrochemical cell and three electrodes. The working electrode (WE) was either a nickel or Inconel foam (supplied by the former Inco Technical Services Ltd.), attached to a Ni wire sealed in a glass tube (Alfa Aesar Puratronic, 0.25 mm in diameter) for electrical contact. The contribution of the Ni wire to the overall surface area, and thus to the electrochemical signal, was less than 1% and assumed to be negligible. Each metal foam WE was degreased with acetone under reflux in order to remove organic impurities. The counter electrode (CE) consisted of high-purity Pt gauze (99.98% in purity, Alfa Aesar) spot-welded to a Pt wire (99.98% in purity, Alfa Aesar) and covered with electro-deposited Pt (Pt black). The surface area of CE was at least ten times larger than that of the WE. The reference electrode (RE) was a reversible hydrogen electrode (RHE); it was made in the same manner as the CE. Hydrogen gas of ultrahigh purity (UHP) (Praxair 5.0 grade) was bubbled through the RE compartment at a pressure of 1 bar. The separation between WE and CE was approximately 3 cm. Electrochemical characterization was carried out in 0.5 M aqueous KOH solution (Sigma-Aldrich KOH pellets of 85% in purity, A.C.S. reagent grade). The electrolyte solution was prepared using UHP water (Millipore, 18.2 MΩ cm). The reference electrode was in electrolytic contact with the main compartment via a Luggin capillary. All potentials are reported with respect to RHE. Prior to each experiment, the electrolyte solution was degassed by bubbling UHP N_2(g) (Praxair 5.0 grade) for 30 min. Throughout the duration of electrochemical measurements, UHP N_2(g) was passed over the electrolyte to maintain the inert gas environment and to expel any gases that might be generated during electrochemical experiments. Glassware was cleaned according to well-established procedures.[15,16] The electrochemical measurements were carried out at a temperature of T = 298 ± 1 K. CV profiles were collected using an Autolab model PGSTAT302 potentiostat (Metrohm). All experimental parameters were controlled, and data was acquired using the NOVA Advanced Electrochemical Software (Metrohm).

Chemical Etching. Nickel develops a native surface oxide (β-$Ni(OH)_2$) upon contact with moist air.[17] For certain experiments, Ni foams were pretreated by chemical etching in order to remove the β-$Ni(OH)_2$ layer and produce a metallic Ni surface. The etching solution employed in this research was made from 30 cm^3 of conc. HNO_3, 10 cm^3 of conc. H_2SO_4, 10 cm^3 of conc. H_3PO_4, and 50 cm^3 of glacial CH_3COOH.[18] The Ni-containing foams were submerged in the solution at T = 298 ± 1 K for a typical etching time of 120 s and then thoroughly rinsed, sonicated, and again rinsed with UHP water.

Electron Microscopy and Focused Ion Beam Characterization. Electron and ion imaging techniques were used to analyze the surface morphology and the 3D structure of the Ni-containing metallic foams. SEM characterization was performed using a Strata DB235 FESEM/FIB instrument operated at 5 kV equipped with an energy dispersive spectrometer (EDS) for elemental analysis (EDAX). FIB experiments were also conducted using a Micrion 2500 instrument (FEI Company). Samples were viewed at varying tilt angles adjusted by moving the SEM stage. A FIB instrument was used to mill and image cross sections of the foams. This instrument employed a focused beam of Ga^+ ions to selectively etch regions of the sample and had the ability to mill with a precision of ca. 1 μm. It was also used to acquire images using secondary ion (SI) and secondary electron (SE) detection modes, which generate different topographical and chemical information. Specimens for the TEM analysis were extracted from the inner wall of the Ni foam with a dual beam FESEM/FIB instrument using an in situ lift-out technique.[19] High resolution TEM and 3D electron tomography (ET) analyses were performed. These measurements were conducted using a Tecnai G2 F20 X-Twin TEM equipped with a Fischione high tilt holder, which allows for tilting of the specimen up to ±80°.

X-ray Photoelectron Spectroscopy Characterization. XPS analysis was carried out using an Analytical Axis Ultra DLD spectrometer (Kratos) equipped with a monochromatic aluminum source (Al Kα 1486.6 eV) operating at a power of 150 W (10 mA emission current and 15 kV voltage). The analysis was conducted on a 700 μm × 300 μm area of the sample. High resolution scans were obtained at a 50 meV step size with a dwell time of 500 ms per step and a pass energy of 20 eV and averaged over 3 scans. The energy scale linearity was calibrated using Al and Mg X-ray sources through the analysis of Ar sputter-cleaned Au and Cu substrates (ISO 15472 procedure). The samples were mounted on the sample holder using a conductive copper tape (EMS). Compositional analysis with depth profiling of the samples was performed by ion etching with an Ar ion beam having energy of 4 kV for specific periods of time.

RESULTS AND DISCUSSION

Electrochemical Characterization of Ni-Containing Foams. CV was used to examine the electrochemical properties of Ni-containing foams in aqueous alkaline electrolyte and to relate such acquired insight to their chemical composition and surface characteristics. A typical CV profile for bulk Ni in aqueous KOH or NaOH solution in the −0.20 to 1.60 V potential (E) range shows the following anodic features: (i) oxidation of metallic Ni to α-$Ni(OH)_2$ at 0.20 < E < 0.40 V (eq 1); (ii) concurrent conversion of α-$Ni(OH)_2$ to β-$Ni(OH)_2$ (eq 2) and oxidation of metallic Ni to β-$Ni(OH)_2$ (eq 3) at 0.50 < E < 1.30 V; (iii) increase of the oxidation state of Ni from +2 to +3 through the oxidation of β-$Ni(OH)_2$ to β-NiOOH at 1.30 < E < 1.55 V (eq 4); and (iv) oxygen evolution reaction (OER) at $E \geq$ 1.55 V (eq 5).[20,21]

$$Ni^0 + 2OH^- \rightarrow \alpha\text{-}Ni(OH)_2 + 2e^- \quad (1)$$

$$\alpha\text{-}Ni(OH)_2 \rightarrow \beta\text{-}Ni(OH)_2 \quad (2)$$

dx.doi.org/10.1021/am401606n | ACS Appl. Mater. Interfaces 2013, 5, 6712−6722

$$Ni^0 + 2OH^- \rightarrow \beta\text{-}Ni(OH)_2 + 2e^- \quad (3)$$

$$\beta\text{-}Ni(OH)_2 + OH^- \rightarrow \beta\text{-}NiOOH + H_2O + e^- \quad (4)$$

$$2OH^- \rightarrow \frac{1}{2}O_2 + H_2O + 2e^- \quad (5)$$

A scan reversal at $E = 1.55$ V generates the following cathodic features: (v) reduction of β-NiOOH to β-$Ni(OH)_2$ at $1.10 < E < 1.40$ V (eq 6) and (vi) hydrogen evolution reaction that gives rise to an appreciable current density at $E < -0.20$ V (eq 7).

$$\beta\text{-}NiOOH + H_2O + e^- \rightarrow \beta\text{-}Ni(OH)_2 + OH^- \quad (6)$$

$$H_2O + e^- \rightarrow \frac{1}{2}H_2 + OH^- \quad (7)$$

In the case of metallic Ni being cycled at $-0.20 < E \leq 0.50$ V in addition to the anodic peak corresponding to the α-$Ni(OH)_2$ formation, there is also a cathodic peak at $-0.12 < E \leq 0.12$ V representing the reduction of α-Ni(OH)2 to Ni^0 (eq 8).

$$\alpha\text{-}Ni(OH)_2 + 2e^- \rightarrow Ni^0 + 2OH^- \quad (8)$$

The β phase of $Ni(OH)_2$ is the most stable and thermodynamically favored oxide of Ni; it is the passive layer that develops on the surface of metallic Ni upon contact with the ambient environment.[21] The conversion of α-$Ni(OH)_2$ to β-$Ni(OH)_2$ is irreversible, and once it has taken place, the cathodic peak corresponding to the reduction of α-$Ni(OH)_2$ is not observed anymore.[18] The reduction of β-$Ni(OH)_2$ cannot be accomplished electrochemically and can be achieved at elevated temperatures in the presence of H_2(g). Alternative methods of preparing a metallic Ni surface involve the removal of the native oxide through chemical etching or mechanical polishing, but these are destructive approaches.

Figure 1 shows two overlaid CV profiles, one for Ni (red line) and the other for Inconel (black line) foams at $-0.15 < E < 1.60$ V in 0.5 M aqueous KOH solution obtained at $T = 298$ K and a potential scan rate of $s = 50$ mV s^{-1}. The anodic and cathodic peaks characteristic of α-$Ni(OH)_2$ formation and reduction are not observed because a layer of β-$Ni(OH)_2$ has developed as the result of several prior CV scans. The most prevalent feature in these CV profiles is the formation and reduction of β-NiOOH and the specific current (I_s, where $I_s = I/m$ and its unit is A kg^{-1} or mA g^{-1}; I is the current and m is the sample mass) increase at $E > 1.50$ V due to the onset of OER. The CV profile for Ni foam displays the same features as those observed for bulk Ni in alkaline media.[21] The CV profile for Inconel foam reveals pronounced differences as compared to the CV profile for Ni foam, especially in the anodic scan. As it is concluded on the basis of spectroscopic measurements (see the section Spectroscopic Analysis of the Chemical Composition of Ni-Containing Foams), the surface of Inconel foam is rich in Ni and the broad anodic peak ($1.18 < E < 1.55$ V) with a shoulder at lower potentials corresponds mainly to the formation of β-NiOOH. Compared to the Ni foam, the peak is shifted toward higher potentials and overlaps the region of OER. The value of I_s for OER is greater than in the case of Ni foam; the specific current for the cathodic feature is greater than in the case of Ni foam, but the difference is small. Nickel and Inconel foams have very different surface morphologies (see the section Surface Morphology of Ni-Containing Foams) and the rough, bubbly surface of Inconel foam gives rise to a larger surface area than Ni foam. Because the ratio I_s(Inconel)/I_s(Ni) ≤ 2 in the OER region and because the real surface area of the Inconel foam is much greater than that of the Ni foam, the results suggest that the Inconel foam is less active toward OER than the Ni foam. The cathodic scans reveal only one, asymmetric peak (reduction of β-NiOOH to β-$Ni(OH)_2$ (eq 6)) for both foams, and their peak potentials and specific currents are comparable. Integration of the cathodic peaks demonstrates that the specific charge (Q_s, where $Q_s = Q/m$ in C kg^{-1} or mC g^{-1}; Q is the peak charge and m is the sample mass) is 592 mC g^{-1} for the Ni foam and 816 mC g^{-1} for the Inconel foam. We observe that the charges under the two cathodic peaks are similar, thus indicating that both samples have similar amounts of β-NiOOH on the surface. Bearing in mind that the difference in Q_s values for Ni and Inconel foams is less than 40% and that Inconel foam has a significantly larger real surface area, we conclude that β-NiOOH does not make up the entire surface of Inconel foam. This behavior is expected because Inconel foams contain other elements within the surface region (see the section Spectroscopic Analysis of the Chemical Composition of Ni-Containing Foams).

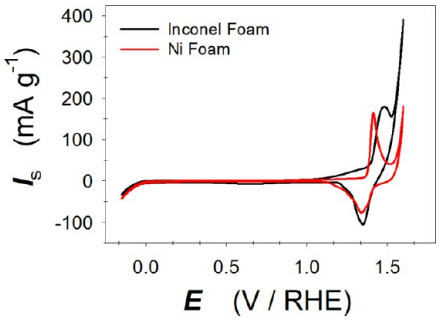

Figure 1. CV profiles of Ni and Inconel foams in 0.5 M aqueous KOH solution obtained at $T = 298$ K and $s = 50$ mV s^{-1} in the $-0.15 \leq E \leq 1.6$ V range. I_s is the specific current.

Inconel foam is a multicomponent material made from Ni, Cr, Mo, Fe, Nb, and Ta (Table 1). Constituent elements such as Cr and Fe display their own electrochemical behavior in alkaline media; thus, the CV profile for Inconel foam cannot be interpreted by considering only the behavior of Ni. Chromium is well-known to segregate to the surface region and to form chemically stable, passive oxide layers, which are not reduced in the cathodic scan.[22−24] Marioli and Soreno[24] compared the electrochemical formation of surface oxides on pure Ni and on Ni−Cr alloy (80%-20%) and observed a larger CV feature in the anodic scan than in the cathodic one for the Ni−Cr alloy. Although Inconel foam is not a true alloy, it gives rise to CV features characteristic of an alloy containing Ni and Cr.

Electrochemically Active Surface Areas of Ni-Containing Foams. Knowledge of the electrochemically active surface area (A_{ecsa}) is important because it specifies the actual surface being in contact with electrolyte and where electron transfer can take place. In the case of Ni materials, estimates of A_{ecsa} and the specific surface area (A_s, where $A_s = A_{ecsa}/m$ in cm^2 g^{-1}) utilize the charge (Q) of the CV peak corresponding to α-$Ni(OH)_2$ formation.[18] The electrochemically active surface area is then determined using eq 9:

$$Q = (q_{Ni(OH)2} \times A_{ecsa}) + (C_{dl} \times A_{ecsa} \times \Delta E) \quad (9)$$

where qNi(OH)$_2$ is the charge density associated with the formation of 1 monolayer (ML) of α-$Ni(OH)_2$ and equals 514

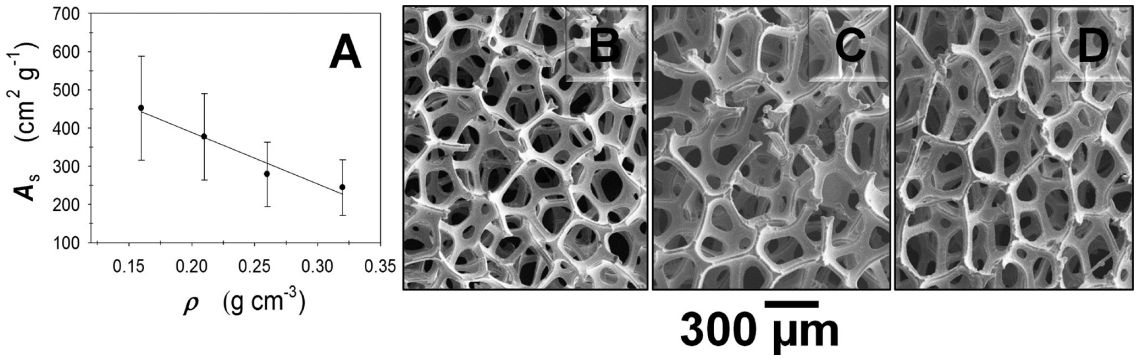

Figure 2. Relationship between the specific surface area (A_s) of etched Ni foams and the bulk density (ρ) of the foam (A). SEM images at a magnification of 125× for Ni foams with various bulk densities: (B) ρ = 0.16 g cm^{-3}; (C) ρ = 0.21 g cm^{-3}; and (D) ρ = 0.32 g cm^{-3}.

μC cm^{-2}, C_{dl} is the double layer capacitance and equals 20 μF cm^{-2}, and ΔE is the CV peak potential range.[25−27] This approach was adopted to determine A_{ecsa} of four Ni foams having different densities. In order to determine A_{ecsa} of each foam, it was first necessary to chemically etch the samples to prepare a metallic surface, which was then oxidized to α-Ni(OH)$_2$. Details of the etching procedure are discussed in a subsequent section (see the section Surface Modification of Ni-Containing Foams through Chemical Etching), but it is important to specify that a fresh etching solution was used for each foam and the etching time was 120 s. Such determined A_{ecsa} values were then used to calculate A_s for each foam.

The manufacturer's material specifications list the Ni foam density in g m^{-2} (Table 1); the thickness of Ni foam sheets is 2.0 mm.[12] Thus, these numbers are converted to bulk density (ρ) values in g cm^{-3} (Table 1). Figure 2A presents a graph of A_s as a function of ρ and reveals that A_s decreases as ρ increases. This trend seems counterintuitive because an increase in mass is expected to enhance the foam surface area, but the SEM images for three Ni foams of different densities (Figure 2B−D) show that their pores are identical in size and the amount of pore space is the same. This behavior is anticipated because the same polyurethane substrate is used to manufacture foams of various densities. The density increase is accomplished by thickening the Ni struts, which results in an overall increase in mass without altering their other characteristics. Table 1 displays the mean value of the strut wall thickness as determined on the basis of FIB cross-section measurements; three FIB cross sections were milled for each type of foam, and the thickness of the strut wall was measured at 5 locations on each cross-section for a total of 15 measurements. The average strut wall thickness increases from ca. 2 μm for the least dense foam to ca. 5 μm for the densest foam. Therefore, the A_{ecsa} values for the various foams are comparable, but their masses gradually increase resulting in a decrease of A_s. The ability to control the density of Ni foams without changing A_{ecsa} is of importance to applications that require very robust materials (e.g., electrodes for large-scale electrolysis). The A_{ecsa} values (Figure 2A) are subject to a large uncertainty that has several origins, as discussed elsewhere.[18] It is difficult to maintain identical fabrication conditions when manufacturing hundreds of square meters of Ni foam in a continuous process.[12] As a result, there are some inherent differences and the thickness of struts and the thickness of native Ni oxide vary from batch to batch. A thorough discussion of different etching solutions and their impact on the 3D structure of Ni foams and A_{ecsa} is reported in our recent paper.[18]

Surface Morphology of Ni-Containing Foams. Figure 3 shows SEM images of Ni, Inconel, and FE2 foams at two levels

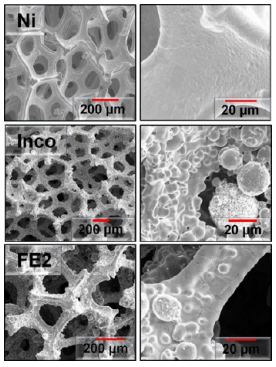

Figure 3. SEM images of Ni, Inconel, and FE2 foams at two levels of magnification showing the porosity of the foams (left column) and their surface morphology (right column).

of magnification. The images in the left-hand column (scale bars of 200 μm) are suitable for evaluating their overall structure, and the images in the right-hand column (scale bars of 20 μm) reveal details of the surface morphology. It is apparent that all of the foams have the same general structure, which resembles a 3D network of roughly pentagonal macroscopic pores and struts ranging in width from 25 to 80 μm. The struts have a concave, triangular shape that is an exact cast of the polyurethane substrate upon which Ni is deposited. Table 1 summarizes the main structural properties of the foams determined from SEM and FIB measurements. The higher magnification images reveal differences in the surface morphology between Ni and multicomponent foams (Inconel and FE2). The surface of Ni foam is smooth with some visible grains and grain boundaries. The surface morphology of Inconel and FE2 foams reveals rough and bubbly surfaces; they have a rougher surface because they are manufactured by binding and annealing metallic powders to a Ni foam substrate. Even after high temperature annealing, the metallic powder particles still retained some of their initial shape. The rough, bubbly surfaces of Inconel and FE2 foams give rise to the large A_{ecsa} reported above.

Structural Characterization of Ni-Containing Foams. The manufacturing process used to fabricate Ni foams leaves a porous metallic material that mimics the structure of the polyurethane foam substrate. The individual macroscopic metallic struts have a 3D structure encompassing the cavity

left behind by the polymer. Figure 4 shows three FIB images for Ni foams at various stages of preparation. Image A presents the

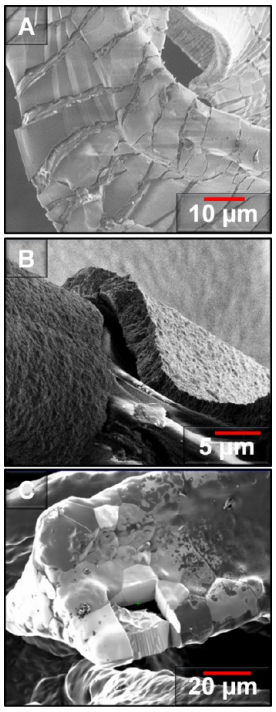

Figure 4. FIB images of Ni foam at various stages of fabrication: (A) polyurethane substrate with a thin layer of PVD Ni; (B) polyurethane substrate with a thick layer of PVD Ni before sintering; and (C) sintered Ni foam.

polyurethane substrate with a very thin layer of Ni prepared by PVD. The Ni deposit is uniform but reveals cracks; the latter develop during handling because the polyurethane foam with a thin layer of Ni is flexible. Image B shows a thick layer of Ni deposit on polyurethane foam prior to the sintering and annealing step. There is a crack in the thick Ni deposit, and one of its sections is lifted showing the polyurethane substrate. The Ni deposit is porous and most likely polycrystalline with a small grain size because FIB images do not reveal any grain structure. Image C shows Ni foam after sintering and burnout. A section of the foam was milled out using a focused beam of Ga^+ ions. The rectangular, milled section exposes a hollow cavity, which once housed the polyurethane template. The Ni deposit looks very different in image C as compared to image B and shows well-defined grains that are clearly visible because they have different crystallographic orientations with respect to the Ga^+ ion beam. We may conclude that the sintering transforms the porous, fine-grained Ni deposit through thermal grain growth.

FIB was used to ion-mill cross-section from struts of Ni and Inconel foams in order to examine their inner structure. These cross sections were used to estimate the thickness of the Ni strut walls for each foam density and to measure the grain size; these parameters are summarized in Table 1. Figure 5 shows four FIB images of cross sections from Ni (images A and B) and Inconel (images C and D) foams. In image B, three features are labeled 1 through 3; 1 corresponds to the hollow cavity; 2 corresponds to an inner porous Ni layer at the interface between the cavity and the Ni strut; and 3 corresponds to a boundary between two metallic grains having different crystallographic orientations. It is much easier to

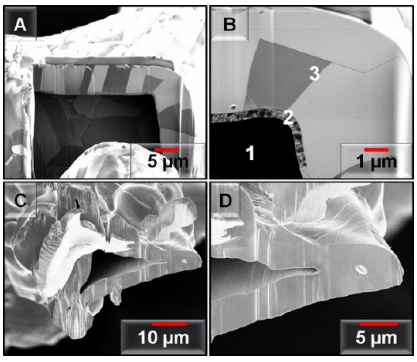

Figure 5. FIB images of cross sections of Ni foam (A and B) and Inconel foam (C and D).

detect the inner, porous layer using ion beam imaging than by SEM, because these two techniques employ different imaging modes. Images C and D demonstrate that Inconel foam has significantly thicker strut walls and that their thickness is less uniform. The fabrication of multicomponent foams (e.g., Inconel, FE2) begins with pure Ni foams on which multicomponent metallic powders are placed using a binding agent and subsequently annealed; thus, it is no surprise that the inner cavity of Inconel foam has similar structural characteristics to those of Ni foam.

The inner, porous wall observed in Ni foams was further investigated using TEM and ET. These measurements were performed on a small section of Ni foam removed from the inner wall of a strut. A FIB instrument was used to prepare the TEM lamella having dimensions ca. 20 μm × 10 μm × 100 nm that was then placed on a specialized tilt manipulator for TEM and ET experiments. A TEM image of the inner, porous wall is shown in the top image of Figure 6; the bottom image shows a 3D ET reconstruction of the inner, porous wall as generated by collecting, aligning, and combining a series of TEM micrographs at various tilt angles. The two images clearly reveal a polycrystalline and granular nanostructure. Combined SEM, TEM, and ET results show that the material has three levels of

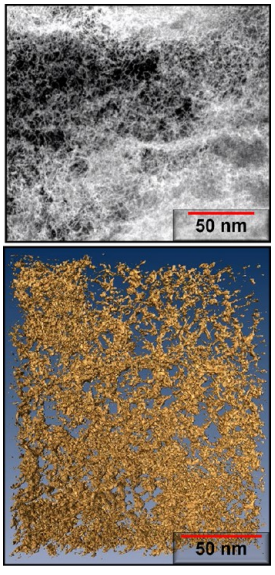

Figure 6. TEM image (top) and ET 3D reconstruction (bottom) of the inner, porous structure present within the struts of Ni foam.

dx.doi.org/10.1021/am401606n | ACS Appl. Mater. Interfaces 2013, 5, 6712−6722

structure and two levels of porosity. The inner nanostructure reported here for the first time is not accessible to electrolyte. However, its discovery suggests that future modification of the fabrication process may be applied to create struts that are entirely nanostructured and possess significantly larger A_s and A_{ecsa}.

Spectroscopic Analysis of the Chemical Composition of Ni-Containing Foams. XPS and EDS were employed to study the chemical composition of Ni and Inconel foams. XPS analysis coupled with Ar^+ ion sputtering was used to provide surface and near-surface chemical composition of these foams at different stages of ion etching. The spectroscopic signal obtained from XPS measurements corresponds to an analysis area of 700 μm × 300 μm. EDS analysis of an area measuring 10 μm × 10 or 20 μm × 20 μm provides information about bulk chemical composition because the signal is generated within 2 μm from the outer surface. Thus, by employing EDS, we probed between 25% and 100% of the struts' depth because their thickness ranges from 2 to 8 μm.

EDS spectra collected from a 10 μm × 10 μm area of a Ni foam strut can be found in the Supporting Information. Only C, O, and Ni are detected; the C and O peaks are small as compared to the Ni peak and are due to the sample transfer via air. The O signal is also present as part of the native surface oxide, β-$Ni(OH)_2$.

Figure 7 presents four XPS survey spectra for Ni foam, which underwent Ar^+ ion etching for various lengths of time ($t_{Ar\text{-}etch}$)

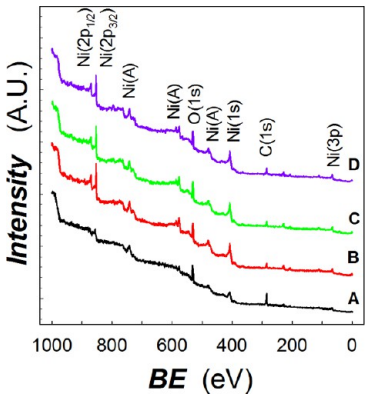

Figure 7. XPS survey spectra of Ni foam exposed to Ar^+ ion etching for various lengths of time: (A) $t_{Ar\text{-}etch}$ = 0 s; (B) $t_{Ar\text{-}etch}$ = 20 s; (C) $t_{Ar\text{-}etch}$ = 40 s; and (D) $t_{Ar\text{-}etch}$ = 80 s.

in the 0 to 80 s range: (spectrum A) $t_{Ar\text{-}etch}$ = 0 s; (spectrum B) $t_{Ar\text{-}etch}$ = 20 s; (spectrum C) $t_{Ar\text{-}etch}$ = 40 s; and (spectrum D) $t_{Ar\text{-}etch}$ = 80 s. The XPS spectra display the peaks that are assigned to the following binding energy (BE) values: C(1s) at 284.7 eV; O(1s) at 531.6 eV; $Ni(2p_{1/2})$ and $Ni(2p_{3/2})$ at 874.2 eV and at 856.3 eV; Ni(3p) at 66.1 eV; one Ni(Auger) peak at 497.0 eV; and several Ni(Auger) peaks in the 800−600 eV range. In the spectrum for $t_{Ar\text{-}etch}$ = 0 s, the O(1s) and C(1s) peaks are more prevalent than after Ar^+ ion etching because C is a surface contaminant and O originates not only from the native β-$Ni(OH)_2$ layer but also from adsorbed H_2O. The intensity of $Ni(2p_{1/2})$ and $Ni(2p_{3/2})$ peaks increases appreciably after the first 60 s of Ar^+ ion etching (spectrum B). The Ni, O, and C XPS signals were studied in detail using high resolution XPS (HRXPS) throughout Ar^+ ion depth profiling. Figure 8 shows HRXPS spectra for the $Ni(2p_{3/2})$ and $Ni(2p_{1/2})$, O(1s), and C(1s) bands for $t_{Ar\text{-}etch}$ = 0, 20, 40, 80,

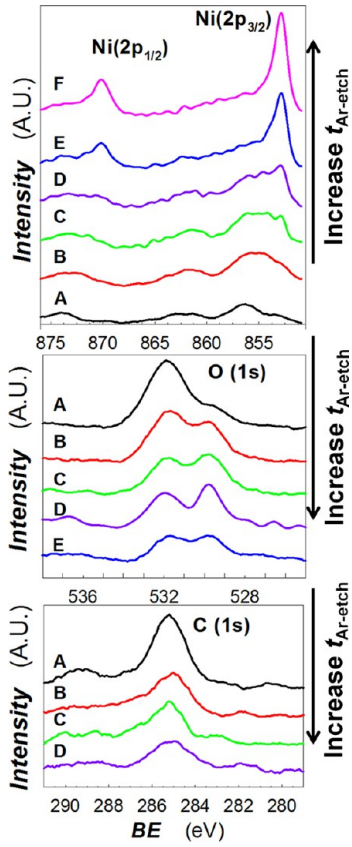

Figure 8. HRXPS spectra of the $Ni(2p_{1/2})$, $Ni(2p_{3/2})$, O(1s), and C(1s) bands for Ni foam exposed to Ar^+ ion etching for various lengths of time: (A) $t_{Ar\text{-}etch}$ = 0 s; (B) $t_{Ar\text{-}etch}$ = 20 s; (C) $t_{Ar\text{-}etch}$ = 40 s; (D) $t_{Ar\text{-}etch}$ = 80 s; (E) $t_{Ar\text{-}etch}$ = 160 s; and (F) $t_{Ar\text{-}etch}$ = 320 s.

160, and 320 s, respectively. The HRXPS signals for $Ni(2p_{1/2})$ and $Ni(2p_{3/2})$ increase steadily as $t_{Ar\text{-}etch}$ is extended. The $Ni(2p_{3/2})$ peak contains contributions from both the Ni(0) and the Ni(2+) oxidation states. The contribution from Ni(0) is observed at a binding energy of BE = 852.7 eV, with a satellite peak at BE = 857−858 eV. The contribution from Ni(2+) is present at BE = 855−856 eV, with a satellite peak at BE = 861 eV.[18,22,28] In spectrum A, the small $Ni(2p_{3/2})$ peak at BE = 856 eV indicates that mostly the Ni(2+) oxidation state is present. As Ar^+ ion etching proceeds for 20 and 40 s, the $Ni(2p_{3/2})$ signal at BE = 856 eV increases because H_2O and CO_2 become desorbed from the Ni foam surface. As the Ar^+ ion etching continues for 80, 160, and 320 s, the $Ni(2p_{3/2})$ peak continues to grow but also shifts toward lower BE values until it reaches a value of BE = 853 eV. This shift in BE indicates that the contribution of Ni(0) increases relative to the contribution of Ni(2+) because the native surface oxide is removed. The conversion of $t_{Ar\text{-}etch}$ to the thickness of the sputtered material is not straightforward for porous materials. Argon ion bombardment erodes polycrystalline Ni with a rate of 13 nm min^{-1}, when a potential of 10 kV is applied.[29] If the sputter rate of 13 nm min^{-1} were employed to the native oxide layer on Ni foams, then $t_{Ar\text{-}etch}$ = 320 s would correspond to the erosion of about 70 nm of the material. In our case, Ar^+ ion bombardment is accomplished by applying a voltage of 3 kV when sputtering Ni foams and 4 kV when sputtering Inconel foams. Because the application of a lower voltage reduces the erosion rate, we may conclude that the thickness of the removed native oxide does not exceed 70 nm and is most likely significantly lower. Because

dx.doi.org/10.1021/am401606n | ACS Appl. Mater. Interfaces 2013, 5, 6712−6722

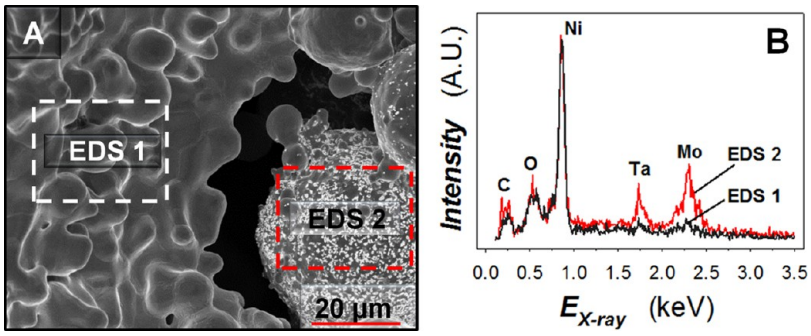

Figure 9. SEM image of Inconel foam (A) and EDS spectra (B) corresponding to two areas designated in the SEM image.

the Ni-containing foams are not flat, the Ar^+ ion beam reaches different parts of the 3D structure at different angles of incidence and gives rise to different sputter rates. Inner portions of the foams are blocked from the Ar^+ ions (shadow effect) and remain covered with the native oxide. Due to the porous nature of Ni-containing foams and the above-mentioned limitations, it is impossible to precisely determine the thickness of the native oxide layer on their surfaces and only an estimate is provided.

Figure 8 presents HRXPS spectra for the O(1s) band as a function of $t_{Ar\text{-}etch}$. The O(1s) band at BE = 528−534 eV has contributions from O in different chemical environments:[22,28] O in the form of H_2O gives rise to a peak at BE = 533 eV, O from $Ni(OH)_2$ at BE = 531.5 eV, and O from NiO at BE = 529.5 eV.[22,28] The O(1s) band shifts toward lower BE values as the duration of Ar^+ ion etching progresses. The broad peak in spectrum A at BE = 532 eV is assigned to H_2O and $Ni(OH)_2$, and the small shoulder at BE = 529.5 eV is assigned to NiO. The spectra B, C, and D display two overlapping peaks with maxima at BE = 531.8 and BE = 529.8 eV, respectively; the first peak is assigned to $Ni(OH)_2$ and the other to NiO. The intensity of the O(1s) peak in spectrum E (for $t_{Ar\text{-}etch}$ = 160 s) is significantly lower, indicating that a majority of H_2O, $Ni(OH)_2$, and NiO is removed from the surface.

Figure 8 also presents a HRXPS spectrum for the C(1s) peak at BE = 284.7 eV for different $t_{Ar\text{-}etch}$ values. The HRXPS spectra display a decrease in the intensity of the C(1s) peak because Ar^+ ions clean the surface (C originates from sample transfer via air); however, even after 80 s of Ar^+ ion etching (spectra D), there is still a detectable C(1s) signal. Because Ni-containing foams are porous materials, it is conceivable that some of the carbon detected by XPS originates from inner struts that are not etched with Ar^+ ions.

It is important to discuss some possible experimental limitations that are unique to the analysis of micro- and nanostructured materials. The design of a surface analysis instrument is such that an X-ray gun, an electron energy analyzer, and an Ar^+ ion gun are permanently mounted at different angles to each other and to the sample. In the case of a flat sample, the focal point of the three devices is the same and the emitted photoelectrons originate from a very thin surface region (1−2 nm). When the sample is irregular and has extended 3D structure, the geometry of the three devices is not ideally optimized anymore and slightly different sections of the sample are analyzed and sputtered. The porous nature of the material explains why the O(1s) and C(1s) peaks are observed even after prolonged Ar^+ ion etching.

Surface chemical analysis of Inconel foam is more complicated than that of Ni foam because Inconel foam has several constituents, and each of them can be either in a metallic state or present as a compound. We employed EDS and XPS to examine the bulk and surface chemical composition of Inconel foam. Figure 9 shows an SEM image of Inconel foam and two EDS spectra from regions having different morphologies. The white box corresponds to a typical strut having a bubbly but smooth surface, and the red box corresponds to a sphere of material attached to a strut; the sphere has characteristic small bright flecks. In general, areas which appear bright in an SEM image correspond to heavy materials that scatter more electrons. Because the bright flecks appear only in certain regions, the SEM images indicate that either the heavy elements never mixed with other constituents or that the heavy elements underwent segregation during the fabrication process. Thus, we may conclude that the composition of Inconel foam is inhomogeneous. The EDS spectra collected from the strut and the sphere demonstrate that the latter is enriched in Ta and Mo; these two constituents of Inconel are barely observed in the spectrum collected from the strut. Although the name "Inconel" refers to a class of alloys containing Ni and Cr, our results suggest that the Inconel foam does not have the same uniform distribution of elements as bulk Inconel alloys. Consequently, Inconel foam is not a true alloy.

XPS and Ar^+ ion depth profiling were employed to analyze the surface and near-surface chemical composition of Inconel foam. Figure 10 presents six XPS survey spectra for various Ar^+ ion etching times in the 0 to 100 s range: (spectrum A) $t_{Ar\text{-}etch}$ =

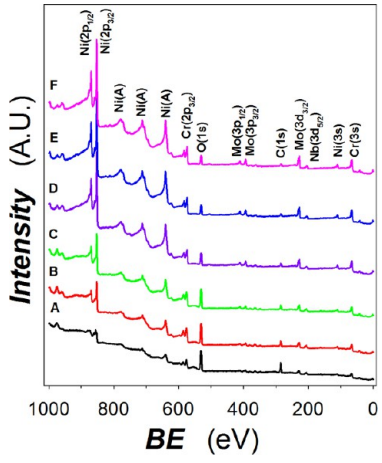

Figure 10. XPS survey spectra of Inconel foam exposed to Ar^+ ion etching for various lengths of time: (A) $t_{Ar\text{-}etch}$ = 0 s; (B) $t_{Ar\text{-}etch}$ = 5 s; (C) $t_{Ar\text{-}etch}$ = 10 s; (D) $t_{Ar\text{-}etch}$ = 30 s; (E) $t_{Ar\text{-}etch}$ = 70 s; and (F) $t_{Ar\text{-}etch}$ = 100 s.

0 s; (spectrum B) $t_{Ar\text{-}etch}$ = 5 s; (spectrum C) $t_{Ar\text{-}etch}$ = 10 s; (spectrum D) $t_{Ar\text{-}etch}$ = 30 s; (spectrum E) $t_{Ar\text{-}etch}$ = 70 s; and (spectrum F) $t_{Ar\text{-}etch}$ = 100 s. They display peaks that are assigned as follows: C(1s) at 284.7 eV; O(1s) at 531.6 eV; Ni($2p_{1/2}$) and Ni($2p_{3/2}$) at 874.2 eV and at 856.3 eV; Ni(3s) at 110.5 eV; Cr($2p_{1/2}$) and Cr($2p_{3/2}$) at 583.4 and 574.2 eV; Cr(3s) at 68.1 eV; Mo($3p_{1/2}$) and Mo($3p_{3/2}$) at 410.6 and 394.8 eV; Mo($3d_{3/2}$) at 228.4 eV; Nb($3d_{5/2}$) at 204.4 eV; and several Ni(Auger) peaks in the 800−600 eV range. Iron is a component of Inconel and as such should be detected using XPS. However, the Fe(2s) band at 845 eV falls very near the Ni($2p_{3/2}$) band, and the Fe($2p_{3/2}$) band at 707 eV overlaps one of the Ni(Auger) peaks; thus, there is no compelling evidence for its presence or absence on the basis of XPS measurements. Cobalt and tantalum are also as components of Inconel; however, there is no XPS evidence for the presence of these elements. We cannot confirm that Co is absent because its XPS peaks overlap with Ni(Auger) peaks. As in the case of Ni foam, the spectrum for $t_{Ar\text{-}etch}$ = 0 s (spectrum A) reveals O(1s) and C(1s) peaks that are more prevalent than after Ar^+ ion etching (spectra B through F) because C is a surface contaminant and O originates from several surface oxides and adsorbed H_2O. The intensity of the peaks corresponding to Ni, Cr, Mo, and Nb increases appreciably after 30 s of Ar^+ ion etching and then levels off. HRXPS spectra were collected for the Ni($2p_{3/2}$), Cr($2p_{1/2}$), and Cr($2p_{3/2}$) bands for each $t_{Ar\text{-}etch}$ and are presented in Figure 11; the spectra A through F refer to the same $t_{Ar\text{-}ion}$ values as in Figure 10. The intensity of the Ni($2p_{3/2}$) peak increases within the initial 30 s of Ar^+ ion etching and then levels off. Unlike in the case of Ni foam, there is practically no change in BE of the Ni($2p_{3/2}$) peak brought about by the Ar^+ ion etching. In spectrum A, the peak centers at BE = 852.7 eV and in spectrum F at BE = 853.1 eV; thus, the entire peak shift is less than 0.5 eV. The binding energy of the Ni($2p_{3/2}$) peak is very close to the characteristic value for metallic Ni, i.e., BE = 853.5 eV. Metallic Ni is also expected to yield a peak at BE = 859 eV. This feature is observed in spectra D, E, and F but not in spectra A through C. Spectrum A shows a small peak at BE = 856 eV that is characteristic of Ni(2+) but disappears already after 5 s of Ar^+ ion etching. On the basis of HRXPS measurements, we may conclude that Ni within Inconel foam is present mostly as Ni(0) with a small amount of Ni(2+) on the foam surface.

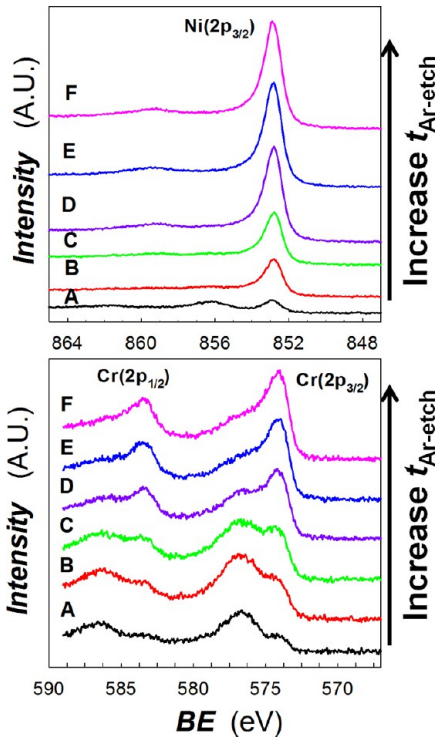

Figure 11. HRXPS spectra of the Ni($2p_{3/2}$), Cr($2p_{1/2}$), and Cr($2p_{3/2}$) bands for Inconel foam exposed to Ar^+ etching for various lengths of time: (A) $t_{Ar\text{-}etch}$ = 0 s; (B) $t_{Ar\text{-}etch}$ = 5 s; (C) $t_{Ar\text{-}etch}$ = 10 s; (D) $t_{Ar\text{-}etch}$ = 30 s; (E) $t_{Ar\text{-}etch}$ = 70 s; and (F) $t_{Ar\text{-}etch}$ = 100 s.

High resolution spectra of the Cr($2p_{1/2}$) and Cr($2p_{3/2}$) bands are shown in Figure 11. The Cr($2p_{3/2}$) band appears as two overlapping peaks with BE = 576.9 and BE = 574.0 eV corresponding to Cr(3+) in the form of Cr_2O_3 and Cr(0), respectively. The Cr($2p_{1/2}$) band also appears as two overlapping peaks with BE = 586.4 and BE = 583.4 eV that also correspond to Cr(3+) and Cr(0).[22,30,31] The intensity of the Cr(3+) peaks decreases and that of Cr(0) increases as Ar^+ ion etching progresses. This evolution of XPS spectra is attributed to the removal of Cr_2O_3, which forms naturally on metallic Cr upon its contact with the ambient. The presence of Cr_2O_3 on the surface of Inconel foam is important because Cr-rich metallic alloys are known to offer corrosion resistance. Chromium is also known to form $Cr(OH)_3$ as a surface compound giving rise to an XPS peak at BE = 578 eV.[22,31] Contributions from Cr_2O_3 and $Cr(OH)_3$ to the XPS spectra cannot be separated only on the basis of Cr($2p_{3/2}$) band measurements because their respective peaks overlap. However, we may conclude that Cr within Inconel foam is present mostly as Cr(3+) with a small amount of Cr(0) on the foam surface.

Surface Modification of Ni-Containing Foams through Chemical Etching. Chemical etching was applied to remove β-$Ni(OH)_2$ from the surface of Ni foam without altering its 3D structure.[18] For bulk Ni materials, typical methods of removing β-$Ni(OH)_2$ are polishing, sand-blasting, ion etching, and chemical etching. Mechanical methods are inapplicable to microstructured and porous materials. A reliable chemical etching procedure for removing β-$Ni(OH)_2$ from Ni foam with minimal alteration to the microstructure is described elsewhere.[18,32,33] SEM images show that chemical etching results in roughening of the surface of the Ni foam struts and occurs preferentially at grain boundaries (see Supporting Information). The images also reveal that chemical etching for short periods of time does not cause any damage to the material and preserves its unique microstructure.

Figure 12 presents a series of CV profiles collected in the α-$Ni(OH)_2$ potential region ($-0.15 \le E \le 0.55$ V) at T = 298 K and s = 100 mV s^{-1} for the same electrode that was etched in intervals for a total t_{etch} = 235 s. The experimental procedure was as follows: (i) the first chemical etching was performed for t_{etch} = 130 s and a CV profile was recorded; (ii) the second etching was performed for an additional 30 s for a total t_{etch} = 160 s and a CV profile was recorded; and (iii) the experiment continued in this manner up to a cumulative t_{etch} = 235 s. Continuous chemical etching results in a faster removal of β-$Ni(OH)_2$ than etching in intervals and that an etching time of t_{etch} = 120 s produces the same final result as etching in intervals for a longer overall time.[18] This observation indicates that the chemical etching of Ni foam requires a certain incubation time.

The CV profiles in Figure 12 reveal α-$Ni(OH)_2$ formation and reduction features, which increase in size as the cumulative

dx.doi.org/10.1021/am401606n | ACS Appl. Mater. Interfaces 2013, 5, 6712−6722

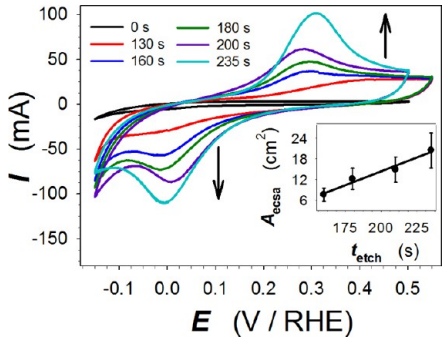

Figure 12. CV profiles for a Ni foam electrode at various chemical etching times (t_{etch} = 0, 130, 160, 180, 200, and 235 s) collected in 0.5 M aqueous KOH solution at T = 298 K and s = 100 mV s^{-1} in the α-$Ni(OH)_2$ potential region. The inset shows the relationship between the electrochemically active surface area (A_{ecsa}) of etched Ni foam and the etching time (t_{etch}).

t_{etch} increases. The α-$Ni(OH)_2$ formation CV features were used to determine the surface area of metallic Ni generated by chemical etching; it is equivalent to A_{ecsa} and is plotted as a function of t_{etch} in the inset of Figure 12. The A_{ecsa} values were only calculated for t_{etch} > 160 s because in the case of shorter t_{etch} this CV feature was too small and its integration would result in large uncertainty. There is a linear increase in A_{ecsa} with extension of t_{etch} for two reasons: (i) more of the native oxide is removed generating a greater portion of metallic surface and (ii) chemical etching increases the surface roughness.

The chemical etching of mutli-element Ni-containing foams is challenging because each metal has its own reactivity with the etching solution and, thus, dissolves at a different rate. The objectives of chemical etching of Ni foams are to: (i) obtain a metallic surface; (ii) increase the surface area through roughening; (iii) activate the Ni foam for application as an electrode material; and (iv) determine A_{ecsa}. In the case of multicomponent Ni-containing foams, the objective (iv) cannot be accomplished because a single electrochemical reaction that can probe the surface area of each component does not exist. We exposed Inconel and FE2 foams to chemical etching in order to evaluate their stability in a strongly acidic environment. The term Inconel refers to a family of alloys with slightly different compositions and contains Ni as the main element, up to 25% of Cr, Fe, Mo, and Nb, and other metals in varied amounts.[34] The other elements are added to accomplish specific characteristics, such as corrosion resistance, grain structure, high temperature stability, strength hardness, elasticity, and ductility.[13,35−37] Previous research on these acid resistant materials focused on bulk materials that were true alloys. Since Inconel and FE2 foams are not true alloys, their behavior in strongly acidic solutions cannot be easily related to the behavior of analogous bulk materials.

The applicability of the above-mentioned solution as an etching medium was examined by submerging in it Inconel foam specimens at three temperatures, namely, T = 293, 313, and 353 K. In the case of T = 293 K, there was no visible degradation of the material over the course of even several days, and the etching solution remained colorless. Chemical etching at T = 313 K resulted in gradual dissolution of the material within 700 s, and the etching solution gradually developed a yellowish green coloration characteristic of Ni and Cr ions in an aqueous medium. We also observed that the degree of Inconel foam dissolution depended on the etching duration and, in general, the longer the time, the greater is the degree of its dissolution. Figure 13 shows FIB images of Inconel foam for

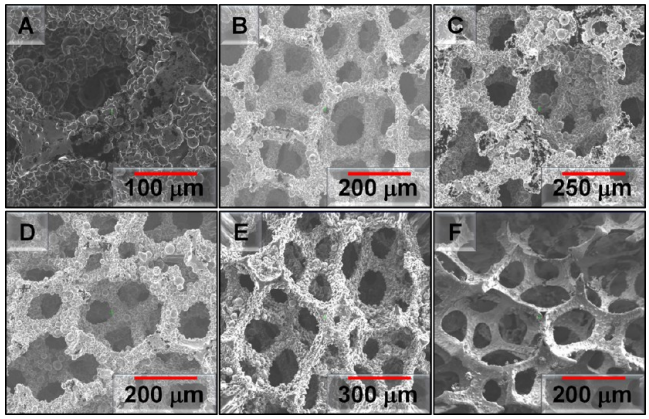

Figure 13. FIB images of Inconel foam exposed to chemical etching for various lengths of time: (A) t_{etch} = 0 s; (B) t_{etch} = 30 s; (C) t_{etch} = 60 s; (D) t_{etch} = 80 s; (E) t_{etch} = 240 s; and (F) t_{etch} = 600 s.

several values of t_{etch} that reveal progression of the evolution of surface morphology and 3D structure during chemical etching. The six pictures refer to the following etching times: image A, t_{etch} = 0 s (no chemical etching); image B, t_{etch} = 30 s; image C, t_{etch} = 60 s; image D, t_{etch} = 80 s; image E, t_{etch} = 240 s; and image F, t_{etch} = 600 s. Images B, C, and D demonstrate that there is no visible degradation of Inconel foam structure within the initial 80 s of etching. Image E reveals that in the case of t_{etch} = 240 s the struts become thinner and their surface smoother. Image F shows that in the case of t_{etch} = 600 s there is an extensive damage to the 3D structure of Inconel foam and its surface morphology is significantly changed; we observe complete dissolution of some struts and thinning of the remaining ones. The resultant structure is no longer an extended network of interconnected struts with pentagonal openings. The sample shown in image F was the last recoverable sample of Inconel foam upon chemical etching because further extension of t_{etch} led to a loss of structural integrity. In the case of chemical etching at T = 353 K, immersion of Inconel foam in the etching solution resulted in an immediate and intense dissolution of the material.

Similarly to Inconel, FE2 alloy was developed to withstand strongly oxidizing environments.[13] Although the compositions of these two alloys are alike (Table 1), the main difference between them is that FE2 contains Al but lacks Mo, Ta, or Nb. The addition of Al enables the material to form a passive alumina (Al_2O_3) layer on the alloy surface, which contributes to its long-term oxidation resistance in gaseous environments.[13] We tested the stability of FE2 foam in the etching solution as an example of a strongly oxidizing environment. Chemical etching of FE2 was studied at T = 293 K because at this temperature FE2 dissolved readily, as indicated by a change in the color of the solution from colorless to green; thus, heating was not required to initiate the etching process. Figure 14 presents three FIB images of FE2 foam at various stages of chemical etching: image A for t_{etch} = 0 s (no chemical etching); image B for t_{etch} = 120 s; and image C for t_{etch} = 240 s. After 120 s of chemical etching (image B), there is severe damage to the foam structure; the bubbly surface morphology disappears, struts become thinner, and the 3D network of struts is partially

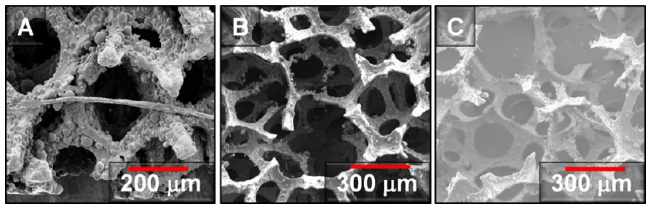

Figure 14. FIB images of FE2 exposed to chemical etching for various lengths of time: (A) t_{etch} = 0 s; (B) t_{etch} = 120 s; and (C) t_{etch} = 240 s.

damaged. After 240 s of chemical etching (image C), entire struts are dissolved and the structure is almost completely broken down; at this point, the sample barely holds together during rinsing with deionized water. Attempts of etching of FE2 foam at higher temperatures than 293 K resulted in the complete dissolution of the foam in less than 30 s.

CONCLUSIONS

The new results presented in this manuscript and their analysis contributes to a greater understanding of Ni-containing foams, which are important materials in electrochemical technologies. Cyclic voltammetry can be used to examine the electrochemical properties of Ni-containing foams in aqueous alkaline media. The electrochemical behavior of Ni foam is similar to that of bulk Ni, and the electrochemical behavior of Inconel foam is similar to that of an alloy containing Ni and Cr. Application of CV to chemically etched Ni foams of various densities allows the determination of their A_{ecsa}; the values of A_{ecsa} are in the 250−450 cm^2 g^{-1} range. SEM images of Ni, Inconel, and FE2 foams show similar 3D structures comprising interconnected struts (25−80 μm in width); the 3D network mimics the pentagonal arrangement of the polyurethane template. Correlation of CV and SEM data reveals that the Ni foams possessing different densities and A_{ecsa} values have similar 3D structures and pore volumes; the increase in Ni foam density is related to the increase of strut wall thickness. The struts within Ni foams are smooth with visible metallic grains, whereas the struts within Inconel and FE2 foams have rough and bubbly surfaces. Although in the case of Inconel and FE2 foams A_{ecsa} cannot be determined using CV, the analysis of SEM and FIB images leads to the conclusion that these two foams have higher values of A_{ecsa} than those of Ni foams. Both EDS and XPS analyses of Ni foam detected only Ni, O, and C; the latter two were present as adsorbed H_2O and CO_2 on the surface of the foam. Some O is also assigned to β-$Ni(OH)_2$ covering the material. HRXPS coupled with Ar^+ ion etching shows that the surface of untreated Ni foam is almost entirely covered with β-$Ni(OH)_2$. Etching of Ni foams with Ar^+ ions removes the surface layer of β-$Ni(OH)_2$ and exposes the underlying metal. SEM and EDS analyses of Inconel foam demonstrate that different surface regions have different chemical compositions. Two constituents, Ta and Mo, are nonuniformly distributed and accumulate preferentially on spheres attached to struts. Thus, Inconel foam is not a true alloy. HRXPS measurements coupled with Ar^+ ion etching reveal that in the case of Inconel foam Ni is present mostly as Ni(0) with a small amount of Ni(2+), whereas Cr is present mostly as Cr(3+) with a small amount of Cr(0). Chemical etching can be successfully applied to pretreat Ni-containing foams without destroying their 3D structure. It increases the strut surface roughness of Ni foams but decreases the strut surface roughness of Inconel and FE2 foams. Chemical etching of Ni foams is required in order to determine the A_{ecsa} of the Ni. FIB can be effectively employed to image Ni-containing foams at various stages of their fabrication and to monitor changes in the materials' porosity, crystallinity, and dimensions. FIB can also be employed to prepare cross sections, which are then used to measure the thickness of strut walls and to analyze the inner wall structure. FIB reveals the existence of inner nanostructure that can be further examined by TEM and ET. Nickel, Inconel, and FE2 foams have a unique structure encompassing pentagonal macropores within 3D network of struts, hollow cavities within struts, and nanostructured inner walls. Thus, we conclude that Ni-containing foams have three levels of structure and two levels of porosity. In conclusion, this contribution is a very comprehensive analysis of Ni-containing foams that discusses their materials science, surface science, and electrochemical characteristics.

ASSOCIATED CONTENT

Supporting Information

Nickel foam morphology prior to and after chemical etching. This material is available free of charge via the Internet at http://pubs.acs.org.

AUTHOR INFORMATION

Corresponding Author

*E-mail: gregory.jerkiewicz@chem.queensu.ca.

Notes

The authors declare no competing financial interest.

ACKNOWLEDGMENTS

The authors gratefully acknowledge financial support towards this project from the Natural Science and Engineering Research Council of Canada (Discovery, Strategic and Equipment Grants), the Canada Foundation for Innovation (Infrastructure Project at Queen's University), and the Canada Research Chairs Program (B.D. Gates). This work made use of 4D LABORATORIES shared facilities supported by the Canada Foundation for Innovation (CFI), British Columbia Knowledge Development Fund (BCKDF), Western Economic Diversification Canada, and Simon Fraser University. They also acknowledge support from VALE (formerly Vale-Inco) and discussions with their personnel, Drs. V. Paserin and Q. Yang. They thank Dr. S. Reyntjens of FEI for specimen preparation.

ABBREVIATIONS

A_{ecsa}, electrochemical surface area
A_s, specific surface area
BE, binding energy
C_{dl}, double layer capacitance
CE, counter electrode
CV, cyclic voltammetry
CVD, chemical vapor deposition
E, potential
EDS, energy dispersive X-ray spectroscopy
ET, electron tomography
FIB, focused ion beam
HRXPS, high-resolution X-ray photoelectron spectroscopy
I_s, specific current
ML, monolayer
Ni(poly), polycrystalline nickel
OER, oxygen evolution reaction
PVD, physical vapor deposition

Q, charge
Q_s, specific charge
$q_{Ni(OH)2}$, charge density for the formation of one monolayer of α-$Ni(OH)_2$
RE, reference electrode
RHE, reversible hydrogen electrode
s, scan rate
SE, secondary electron
SEM, scanning electron microscopy
SI, secondary ion
T, temperature
$t_{Ar\text{-}etch}$, Ar ion etch time
t_{etch}, chemical etch time
TEM, transmission electron microscopy
UHP, ultrahigh purity
WE, working electrode
XPS, X-ray photoelectron spectroscopy
3D, three-dimensional
ρ, bulk density

REFERENCES

(1) Watanabe, K.; Kikuoka, T. *J. Appl. Electrochem.* **1995**, *25*, 219−226.
(2) Montillet, A.; Comiti, J.; Legrand, J. *J. Appl. Electrochem.* **1993**, *23*, 1045−1050.
(3) Simon, P.; Gogotsi, Y. *Nat. Mater.* **2008**, *7*, 845−854.
(4) Kleperis, J.; Wójcik, G.; Czerwinski, A.; Skowronski, J.; Kopczyk, M.; Beltowska-Brzezinska, M. *J. Solid State Electrochem.* **2001**, *5*, 229−249.
(5) Chyrkin, A.; Schulze, S. L.; Piron-Abellan, J.; Bleck, W.; Singheiser, L.; Quadakkers, W. *J. Adv. Eng. Mater.* **2010**, *12*, 873−883.
(6) Fleischmann, M.; Korinek, K.; Pletcher, D. *J. Chem. Soc., Perkin Trans 1* **1972**, *2*, 1396−1403.
(7) Motheo, A. J.; Machado, S. A. S.; Rabelo, F. S. B.; Santos, J. R. J. *J. Braz. Chem. Soc.* **1994**, *5*, 161−165.
(8) Norskov, J. K. *Nature* **2001**, *414*, 405−406.
(9) Robertson, P. M. *J. Electroanal. Chem.* **1980**, *111*, 97−104.
(10) Banhart. *J. Prog. Mater. Sci.* **2001**, *46*, 559−632.
(11) Brown, I. J.; Sotiropoulos, S. *J. Appl. Electrochem.* **2001**, *31*, 1203−1212.
(12) Paserin, V.; Marcuson, S.; Shu, J.; Wilkinson, D. S. *Adv. Eng. Mater.* **2004**, *6*, 454−459.
(13) Walther, G.; Kloden, B.; Buttner, T.; Weissgarber, T.; Kieback, B.; Bohm, A.; Naumann, D.; Saberi, S.; Timberg, L. *Adv. Eng. Mater.* **2008**, *10*, 803−811.
(14) Kummer, M.; Kirchhoff, J. R. *Anal. Chem.* **1993**, *65*, 3720−3725.
(15) Conway, B. E.; Angerstein-Kozlowska, H.; Sharp, W. B. A.; Criddle, E. E. *Anal. Chem.* **1973**, *45*, 1331−1336.
(16) Angerstein-Kozlowska, H. *Surfaces, Cells, and Solutions for Kinetic Studies*; Yeager, E., Ed.; Comprehensive Treatise of Electrochemistry Vol. *9*; Plenum Press: New York, 1984.
(17) Oliva, P.; Leonardi, J.; Laurent, J. F.; Delmas, C.; Braconnier, J. J.; Figlarz, M.; Fievet, F.; de Guibert, A. *J. Power Sources* **1982**, *8*, 229−255.
(18) Grden, M.; Alsabet, M.; Jerkiewicz, G. *ACS Appl. Mater. Interfaces* **2012**, *4*, 3012−3021.
(19) Giannuzzi, L. A.; Kempshall, B. W.; Schwarz, S. M.; Lomness, J. K.; Prenitzer, B. I.; Stevie, F. A. *FIB Lift-Out Specimen Preparation Techniques*; Giannuzzi, L. A., Stevie, F. A., Eds.; Introduction to Focused Ion Beams; Springer: New York, 2005.
(20) Alsabet, M.; Grden, M.; Jerkiewicz, G. *Electrocatalysis* **2011**, *2*, 317−330.
(21) Jouanneau, A.; Keddan, M.; Petit, M. C. *Electrochim. Acta* **1976**, *21*, 287−292.
(22) Addari, D.; Elsener, B.; Rossi, A. *Electrochim. Acta* **2008**, *53*, 8078−8086.
(23) Garretsen, J. H.; de Wit, J. H. W. *Corros. Sci.* **1990**, *30*, 1075−1084.
(24) Marioli, J. M.; Sereno, L. E. *Electrochim. Acta* **1994**, *40*, 983−989.
(25) Conway, B. E.; Bai, L. *J. Electroanal. Chem.* **1986**, *198*, 149−175.
(26) Lasia, A.; Rami, A. *J. Electroanal. Chem.* **1990**, *294*, 123−141.
(27) Machado, S. A. S.; Avaca, L. A. *Electrochim. Acta* **1994**, *39*, 1385−1391.
(28) Kitakatsu, N.; Maurice, V.; Hinnen, C.; Marcus, P. *Surf. Sci.* **1998**, *407*, 36−58.
(29) Okajima, Y. *J. Appl. Phys.* **1980**, *51*, 71−717.
(30) Fairley, N. *CasaXPS Version 2.3.14*; Casa Software Ltd, 2008.
(31) Gupta, R. P.; Sen, S. K. *Phys. Rev. B: Condens. Matter* **1974**, *10*, 71−77.
(32) Payne, B. P.; Biesinger, M. C.; McIntyre, N. S. *J. Electron Spectrosc. Relat. Phenom.* **2011**, *184*, 29−37.
(33) Weininger, J. L.; Breiter, M. W. *J. Electrochem. Soc.* **1963**, *110*, 484−490.
(34) Zoltowski, P. *Electrochim. Acta* **1993**, *38*, 2129−2133.
(35) Azarmi, F.; Saaedi, J.; Coyle, T. W.; Mostaghimi, J. *Adv. Eng. Mater.* **2008**, *10*, 459−464.
(36) Revie, R. W., Ed.; *Uhlig's Corrosion Handbook*; John Wiley & Sons: Hoboken, NJ, USA, 2011; Vol. *3*.
(37) Ashby, M. F.; Jones, D. R. H. *Engineering Materials*; Pergamon Press: Oxford, 1989.